Published in final edited form as:
Neuroimage. 2012 February 1; 59(3): 2560–2568. doi:10.1016/j.neuroimage.2011.08.082.

Morphology Enabled Dipole Inversion for Quantitative Susceptibility Mapping Using Structural Consistency Between the Magnitude Image and the Susceptibility Map

Jing Liu[1,*], **Tian Liu**[1,2,*], **Ludovic de Rochefort**[3], **James Ledoux**[1], **Ildar Khalidov**[1], **Weiwei Chen**[4], **A. John Tsiouris**[1], **Cynthia Wisnieff**[1], **Pascal Spincemaille**[1], **Martin R. Prince**[1], and **Yi Wang**[1,2,5]

[1]Department of Radiology, Weill Medical College of Cornell University, New York, New York, United States

[2]Department of Biomedical Engineering, Cornell University, Ithaca, New York, United States

[3]Imagerie par résonance magnétique médicale et multi-modalités (IR4M), Université Paris-Sud, CNRS, UMR 8081, Orsay, France

[4]Department of Radiology, Tonji Hospital, Tongji Medical College of Huazhong University of Science and Technology, 1095 Jiefang Avenue, Wuhan, China

[5]Department of Biomedical Engineering, Kyung Hee University, Korea

Abstract

The magnetic susceptibility of tissue can be determined in gradient echo MRI by deconvolving the local magnetic field with the magnetic field generated by a unit dipole. This Quantitative Susceptibility Mapping (QSM) problem is unfortunately ill-posed. By transforming the problem to the Fourier domain, the susceptibility appears to be undersampled only at points where the dipole kernel is zero, suggesting that a modest amount of additional information may be sufficient for uniquely resolving susceptibility. A Morphology Enabled Dipole Inversion (MEDI) approach is developed that exploits the structural consistency between the susceptibility map and the magnitude image reconstructed from the same gradient echo MRI. Specifically, voxels that are part of edges in the susceptibility map but not in the edges of the magnitude image are considered to be sparse. In this approach an L_1 norm minimization is used to express this sparsity property. Numerical simulations and phantom experiments are performed to demonstrate the superiority of this L_1 minimization approach over the previous L_2 minimization method. Preliminary brain imaging results in healthy subjects and in patients with intracerebral hemorrhages illustrate that QSM is feasible in practice.

Keywords

quantitative susceptibility mapping; gradient echo; inverse problem; morphology enabled dipole inversion; tissue susceptibility; L_1 norm; L_2 norm; constraint minimization; sparsity

Contact information: Yi Wang, Cornell MRI, 416 East 55th Street, New York, NY, 10022, USA, Phone: 212-752-3936, Fax: 212-421-1844, yiwang@med.cornell.edu.

[*]These authors contributed equally to this work.

Introduction

Quantitatively measuring the magnetic susceptibility of brain tissue has recently received increased scientific and clinical attention (de Rochefort et al., 2008a; de Rochefort et al., 2010; Kressler et al., 2010; Li and Leigh, 2004; Li et al., 2011; Liu, 2010; Liu et al., 2009; Schweser et al., 2010a; Shmueli et al., 2009; Wharton and Bowtell, 2010; Wharton et al., 2010). The magnetic susceptibility of a material is a measure for the amount of magnetization induced in that material when placed in an external magnetic field such as the main magnetic field, B_0, of an MRI scanner. Variation in tissue susceptibility generates the local magnetic field: the field value at any given point in space is the convolution of all surrounding susceptibility sources with the field generated by a unit dipole (Jackson, 1999), which we will refer to in the following as the dipole kernel. The phase data from gradient echo MRI is used to derive the local magnetic field. Quantitative susceptibility mapping (QSM) of tissue requires the deconvolution of this measured magnetic field with the dipole kernel. This inverse problem is ill-posed: the dipole kernel, viewed in the Fourier domain, is zero on a double cone surface that makes a 54.7° angle with the z axis; at each location on this surface, the susceptibility in the Fourier domain can be arbitrarily changed while still producing the same magnetic field (Haacke et al., 2005). Previous approaches for overcoming the ill-posedness include sampling at multiple orientations (Liu et al., 2009), altering the susceptibility reconstruction by truncating the dipole kernel (Shmueli et al., 2009; Wharton et al., 2010) and regularizing the inversion (Kressler et al., 2010). However, these approaches suffer from impracticality, residual artifacts, or systematic bias.

The voxels in the Fourier domain at which the susceptibility can be arbitrarily changed without affecting the resulting magnetic field are only located at a double cone surface. A small amount of additional information may enable the unique determination of susceptibility. Recently, a physical prior based on the structural agreement between the magnitude image and the susceptibility map was reported to be very promising for QSM (de Rochefort et al., 2010). Tissue compartments of reasonably uniform intensities in the magnitude image may most likely represent materials with a uniform susceptibility. This suggests that most susceptibility map edges may be found in the same locations as the magnitude image edges. On the other hand, the edges associated with the streaking artifacts in susceptibility images radiate away from tissue boundaries. Therefore, a physical solution to the QSM problem that is not corrupted by streaking artifacts can be found by minimizing the number of voxels of the susceptibility map gradient that are not on the magnitude image gradient. This approach is referred to as the Morphology Enabled Dipole Inversion (MEDI). Previous work (de Rochefort et al., 2010) used an L_2 norm minimization to formulate the structural agreement between the magnitude image and the susceptibility map. While the L_2 norm minimization is straightforward to implement, it is not a true formulation for sparsity, since it does not effectively reduce the number of non-zero voxels in an image (Candes and Romberg, 2007). It consequently suffers from errors or streaking artifacts caused by slow spatial variations.

Here we describe an L_1 –norm minimization, which is regarded as a good practical alternative to L_0 norm minimization for promoting sparsity, which is the ideal formulation but harder to solve in practice (Candes and Romberg, 2007). Numerical simulations, phantom and human experiments were performed to optimize the parameter settings of the L_1 norm minimization and to demonstrate the improvements over the previous L_2 norm minimization.

Materials and methods

Magnetic susceptibility and field

In MRI, the tissue local magnetic field can be approximated as the convolution of the dipole kernel with the susceptibility distribution (de Rochefort et al., 2008b; Jackson, 1999):

$$\Delta B(r)=\int_{r'\neq r}\chi(r')\frac{3\cos^2(\theta_{r-r'})-1}{4\pi|r'-r|^3}d^3r'=\frac{3\cos^2(\theta_r)-1}{4\pi r^3}\otimes\chi(r) \quad [1]$$

where $\Delta B(r)$ is the local field measured relative to B_0, $\Delta B(r)=(B(r)-B_0)/B_0$, $\chi(r)$ is the spatially varying susceptibility distribution, r and r' refer to the locations of the observed field and susceptibility source respectively, θ_r is the azimuthal angle of r in the spherical coordinate (the subscript r is typically omitted). This forward problem, relating the local magnetic field to the local susceptibility, can be written in matrix form as:

$$b=D\chi, \quad [2]$$

where χ and b denote the vector forms of the spatial susceptibility distribution and the measured local field, D is a matrix representing the convolution with the dipole kernel $3(\cos^2\theta-1)/4\pi r^3$, which is defined as the magnetic field generated by a unit dipole. As matrix D has a very large dimension and is computationally expensive to directly store and apply, the convolution $D\chi$ is executed efficiently as a multiplication in the Fourier domain (Salomir et al., 2003).

Solution with a physical prior

The physical prior in MEDI is expressed by minimizing the number of voxels that belong to edges in the susceptibility map but not edges in the magnitude image. Accordingly, the susceptibility reconstruction is formulated as a constrained L_1 norm minimization problem:

$$\min_\chi\left\|MG\chi\right\|_1 \text{ subject to} \left\|W(D\chi-b)\right\|_2^2\leq\varepsilon. \quad [3]$$

Here, the structural weighting matrix M is derived from the gradient of the magnitude image. G denotes the gradient operator, W is a weighting matrix proportional to the image magnitude to compensate for the noise variation in the field measurement, ε is the noise power and controls the fidelity of the reconstruction to the data. In this preliminary work, the structural weighting M was chosen as a binary mask that assigned zero to the voxels with large gradients in the magnitude image and one to those voxels with small gradients:

$$\mathrm{M}=\begin{cases}0 & |Gm|\geq\mu\\ 1 & |Gm|<\mu\end{cases} \quad [4]$$

where m is the magnitude image in vector form and μ is a threshold related to the image noise level.

Algorithm implementation

This constrained problem, Eq. 3, is reformulated using the Lagrange Multiplier method into the following unconstrained minimization problem, whose solution can be efficiently found using numerical methods:

$$\min_{\chi,\lambda} E(\chi,\lambda), \text{with } E(\chi,\lambda) \equiv \left\|MG\chi\right\|_1 + \lambda\left(\left\|W(D\chi - b)\right\|_2^2 - \varepsilon\right) \quad [5]$$

This unconstrained minimization problem is solved by finding $\begin{cases} \nabla_\chi E(\chi,\lambda)=0 \\ \nabla_\lambda E(\chi,\lambda)=0. \end{cases}$

The cost function E is first minimized by setting its gradient with respect to χ to zero for a given λ value:

$$\begin{aligned} 0=\nabla_\chi E(\chi,\lambda) &= (MG)^H sign(MG\chi) + 2\lambda(WD)^H(WD\chi - Wb) \\ &\equiv L(\chi)\chi - \tilde{b} \end{aligned} \quad [6]$$

where $(\cdot)^H$ denotes the conjugate transpose, $L(\chi)$ denotes $(MG)^H \frac{1}{|MG\chi|} MG + 2\lambda(WD)^H WD$ and $\tilde{b}=2\lambda(WD)^H Wb$. Here, a weak derivative is used for the derivative of the L_1 norm: $\left(\left\|x\right\|_1\right)' = sign(x) = \begin{cases} x/|x| if\ x \neq 0 \\ 0\ if\ x=0 \end{cases}$. One way to solve Eq. 6 is to write it as a fixed point equation (Vogel, 2002) and solve it iteratively:

$$\chi_{n+1} = L^{-1}(\chi_n)\tilde{b} \quad [7]$$

Using $\tilde{b} = L(\chi_n)\chi_n - \nabla_\chi E(\chi_n, \lambda)$ from Eq. 6, the fixed point iteration Eq. 7 is expressed as a quasi-Newton problem (Nocedal and Wright, 2006) that is more robust against roundoff errors. The quasi-Newton approach iteratively approximates the original nonlinear minimization problems using local derivatives (linearization) as a series of quadratic minimization problems. Accordingly, Eq. 7 is reformulated as:

$$\chi_{n+1} = L^{-1}(\chi_n)(L(\chi_n)\chi_n - \nabla_\chi E(\chi_n,\lambda)) = \chi_n - L^{-1}(\chi_n)\nabla_\chi E(\chi_n,\lambda) \quad [8]$$

The update in the quasi-Newton Eq. 8 can be computed using a conjugate gradient method (Hestenes and Stiefel, 1952). In this preliminary study, an initial estimate of χ as $\chi_0=(WD)^H Wb$ was used and iteration was stopped when the relative change $\|\chi_{n+1} - \chi_n\|_2 / \|\chi_n\|_2$ was lower than 10^{-2}.

The zero derivative of the cost function E with respect to the Lagrange multiplier parameter λ leads to a data fidelity constraint that the residual error equals the expected noise power,,

$$\begin{aligned} 0=\nabla_\lambda E(\chi_n,\lambda) &= \left\|W(D\chi - b)\right\|_2^2 - \varepsilon \\ \left\|W(D\chi^* - b)\right\|_2^2 &\approx \varepsilon \end{aligned} \quad [9]$$

where χ^* is the susceptibility solution from Eq. 6 under the given λ. A range of λ values was evaluated to identify a λ value whose corresponding susceptibility solution χ satisfies Eq. 9. The algorithm was implemented in MATLAB (The MathWorks, Natick, MA, USA).

Comparison with L_2 norm minimization

To demonstrate the improvement in susceptibility mapping with the proposed L_1 norm minimization, we also implemented the L_2 norm minimization by replacing the constraint term $\|MG\chi\|_1$ in Eqs.3&5 with $\|MG\chi\|_2{}^2$. The corresponding gradient term then became $\nabla_\chi \|MG\chi\|_2{}^2 = 2(MG)^H(MG)\chi$. The two methods were abbreviated as WL1 and WL2, respectively.

Numerical simulations

A 3D numerical phantom was generated to evaluate the accuracy of the proposed method, to investigate the influence of signal-to-noise-ratio (SNR) and contrast-to-noise-ratio (CNR) of the MR image. A phantom with eight spheres of the same size but with increasing magnetic susceptibilities (linearly ranging from 0.5 ppm to 4.0 ppm) was placed in a background with zero susceptibility (Fig. 1a). A magnitude image (Fig. 1b) was constructed by assigning a uniform and identical signal to each of the eight spheres that was twice that of the background, except for two spheres: one (black arrow in Fig. 1b) mimicking a hemorrhagic lesion of non-zero susceptibility with zero magnitude signal, while the other (white arrow in Fig. 1b) had a signal that was only 30% higher than that of the background. Three small cylindrical tubes were placed perpendicular to each other in the central region of the numerical phantom and were assigned a susceptibility of 0.5 ppm and a magnitude signal equal to 10% of the background signal. The local magnetic field was computed from the described 3D susceptibility distribution according to Eq. 1. The phase map was generated from the local magnetic field using the relationship $\phi = (\gamma B_0 TE)\Delta B(r)$, where ϕ denotes the phase, γ the gyromagnetic ratio, B_0 the field strength (1.5 T), and TE the echo time (4.5 ms). The combination of the simulated image magnitude m and phase ϕ generated a complex MR image, to which complex Gaussian noise n_c was added: $me^{j\phi} + n_c = \tilde{m}e^{j\tilde{\phi}}$. Then, the phase $\tilde{\phi}$ of this noisy complex MR image was used to compute the local magnetic field (shown in Fig. 1c), which was then used as the input for the QSM algorithm. Results with SNR=10 are illustrated as examples.

Susceptibility maps were calculated at various values for the Lagrange multiplier λ to examine dependence of the susceptibility map on λ. Optimality of QSM was defined in terms of the relative error $\|\chi_e - \chi_r\|_2 / \|\chi_e\|_2$ of the reconstructed susceptibility map χ_r with respect to the true susceptibility map χ_e. The residual error was calculated as $\left\|W(D\chi - b)\right\|_2 / \sqrt{N}$, where N is the number of nonzero voxels in W. The eight spheres were chosen as regions of interest (ROIs). To assess accuracy, a linear regression was performed between the reconstructed susceptibilities and the true values.

Phantom experiments

A Gadolinium (Gd) phantom was designed for experimental validation (de Rochefort et al., 2010). Spherical balloons were filled with solutions of various concentrations of Gd-DTPA (Magnevist; Berlex Laboratories, Wayne, NJ), which were immersed in a cylindrical container (diameter 12.5 cm; height 30 cm) filled with water. Gd concentrations ranged between 0.5% and 3.0% with a 0.5% increment, corresponding to susceptibilities of 0.81 ppm, 1.63 ppm, 2.45 ppm, 3.26 ppm, 4.08 ppm, and 4.89 ppm. This Gd-water phantom was imaged on a 1.5T MRI scanner (HDx, GE Healthcare, Waukesha, WI) with the body coil and a multi-echo gradient sequence with FOV=12.8 cm, TR/TEs =30/3.05/4.05/5.05 ms, BW = ±31.2 kHz, flip angle (FA)=30°, and isotropic spatial resolution of 2 mm.

Human study

The human study was approved by our institutional review board. The proposed QSM method was applied to data from nine healthy volunteers and 17 brain trauma patients (four

with brain hemorrhages) using an eight-channel head coil on a 3.0T MRI scanner (HDx, GE Healthcare, Waukesha, WI). A 3D multi-echo gradient echo sequence was used to acquire axial images with FOV = 24cm, spatial resolution = 0.5~1×0.5~1×2~3 mm, BW = ±62.5 kHz, TR= 40ms, TEs =5/10/15/20/25 ms, FA = 20°. Susceptibilities were measured in several brain regions, including the globus pallidus, the substantia nigra, the red nucleus, the vein of galen, and at focal hemorrhages, when present.

MRI data processing

To estimate the field map, a one-dimensional temporal unwrapping of the phase was performed in each voxel followed by a weighted least-squares fit of the temporally unwrapped phases in each voxel over TE (de Rochefort et al., 2008a; Kressler et al., 2010). To address the frequency aliasing on the field map, a magnitude map guided spatial unwrapping algorithm was subsequently applied (Ghiglia and Pritt, 1998). A method based on projection onto dipole fields was used to remove the background field (de Rochefort et al., 2010; Liu et al., 2011a). The threshold μ was determined iteratively such that approximately 30% of the voxels in the gradient of the magnitude image within the ROI were considered edges. This value was determined in this study to provide an adequate balance between streaking artifact suppression and susceptibility map accuracy. For both the numerical and experimental phantoms, λ was gradually reduced from an initial value of 10^4 to a value at which the residual in the data fidelity term matched the expected noise level, which is also referred to as the discrepancy principle (Hansen, 1998). The expected noise level was estimated over a region of background air. For the human data, an optimal λ was determined from one volunteer case (Fig. 4) using the discrepancy principle. Then the same λ was applied to all cases acquired using the same imaging protocol. The regularization parameter λ was determined in the same manner for the WL2 method. The susceptibility value difference between WL1 and WL2 was assessed by t-test with significance determined at $\alpha = 0.01$. Each human brain QSM calculated by WL1 and WL2 was displayed in a random order to an image reader who was blinded to the reconstruction method. Considering streaking artifacts and blurring, the image quality was rated using the following score system: 1 = free of artifacts or blurring, 2 = moderate artifacts or blurring, 3 = severe artifacts or blurring. A paired Wilcoxon rank sum test was performed to determine significant differences in image quality between WL1 and WL2.

Results

Numerical simulations

The Lagrange multiplier λ controlled the fidelity of the reconstructed QSM as demonstrated in Figs. 1d–g. A small λ enforced the minimization of L_1 norm term (Eq. 5), resulting in a smooth map with an underestimation of the susceptibility values of each of the eight spheres (Fig. 1d). The structures with low CNR (the sphere indicated by the white arrow and the small tubes at the center) were barely seen (Fig. 1d), likely because the weighting matrix M imposed the same value as the background. A large λ enforced the data fidelity at the cost of streaking artifacts (Fig. 1f). The optimal λ ~316 for QSM, shown in Fig. 1e and highlighted with a solid black dot in Fig. 1g, corresponded to the minimum relative error (0.175), with a residual error (0.092) close to the simulated noise SD (0.1). The linear regression between the measured and the known susceptibilities in the eight ROIs indicated a high accuracy (slope = 0.98, offset − 0.05 ppm).

QSM reconstructions obtained with L_2 norm minimization method (WL2, Fig. 2a) and L_1 norm minimization (WL1, Fig. 2d) are shown. The regularization parameter λ was 31.6 and 316 for WL2 and WL1, respectively. The WL2 susceptibility in the region with low image CNR had a lower accuracy due to the insufficient definition of edges (white arrows in Figs.

1b&2a and the outlier on Fig. 2c). The WL1 method provided a more accurate susceptibility map with less streaking artifacts (Figs. 2d vs. Figs. 2a) including clearer contours, better accuracy (regression slope was 0.98 versus 0.88), and a smaller relative error (0.175 versus 0.314). The WL1 method generated good precision and accuracy even in regions with reduced magnitude signal and unreliable phase signal (black arrow in Fig. 1b), as well as regions with a poor CNR (white arrow in Fig. 1b). The differences between WL1 and WL2 calculated susceptibility values were statistically significant in the two spheres with either low CNR or SNR (arrows in Fig. 1b) ($P<0.01$), but insignificant in other spheres ($P>0.05$). However, both methods showed errors for the three small tubes with low CNR and susceptibility at the center of the phantom in (Figs. 2d): Their susceptibility values calculated using WL1 and WL2 had similar 36%-46% underestimation.

Phantom experiments

The magnitude image and the field map of the Gd-water phantom (Figs. 3a&d) demonstrated saturation of the magnitude signal with increasing Gd concentration. The local magnetic field disturbance, however, grew larger (particularly outside the balloon) with increasing Gd concentration. Reconstructed susceptibility maps using both WL2 and WL1 (Figs. 3b&e) allowed the quantification of the Gd concentration (Figs. 3c&f). The regularization parameter λ was 10 and 100 for WL2 and WL1, respectively. WL1 provides a higher accuracy than WL2: the regression of the measured versus known susceptibility values showed a slope of 0.97 vs 0.90. The differences between WL1 and WL2 calculated Gd susceptibility values were statistically significant in each of the 6 balloons ($P<0.01$).

Human study

QSM was successfully obtained in all human subjects. Typical susceptibility maps reconstructed with WL2 and WL1 methods in healthy subjects are shown in Fig. 4, which displays the magnitude images (Fig. 4a), field maps (Fig. 4b), QSM with WL2 (Fig. 4c), and QSM with WL1 (Fig. 4d) in three orientations (top: axial; middle: sagittal; bottom: coronal). The regularization parameter λ was 100 and 300 for WL2 and WL1, respectively. There was no statistically significant difference between WL1 and WL2 estimated susceptibility values over the entire brain ($P>0.05$). However, the WL1 method showed regional improvements over the WL2 method in reduction of streaking artifacts. The typical streaking artifacts of dipole kernel undersampling were most pronounced in the sagittal and coronal views (ellipse in Fig 4c, middle) and were visible as rings in the axial view of the WL2 QSM (arrow in Fig. 4c, top), particularly those originating from the brain edges where the field map quality was deteriorated due to low SNR in the magnitude image (arrow in Fig. 4c). These artifacts were markedly reduced in the WL1 QSM (Fig. 4d). The appearance of a right-left vein in the field map (arrow in Fig. 4b, top row) was not easily visible in the magnitude of short TE (=5 ms) and QSM images (Figs. 4a&c&d), suggesting a strong blooming artifact from deoxyhemoglobin in the vein in the neighboring slice, which was confirmed by checking the slice right above it (Fig. 4, second row). Strong susceptibility was found in the globus pallidus (hollow arrow in Fig. 4d) but not in the ventricle (short arrows in Fig. 4d), while both appeared hypointense in the magnitude image (Fig. 4a). Negative susceptibility appeared black in QSM. We observed this oval shape black spot in each ventricle on QSM (short arrow in Fig. 4d), which is consistent with calcium deposition that is known to occur in the choroid plexus.

Fig. 5 displays brain images of a patient with intracerebral hemorrhage (top: axial; middle: coronal; bottom: sagittal). Consistent with the strong paramagnetic susceptibility of iron in the blood products (ferritin and hemosiderin) of the hemorrhage (Bradley, 1993; Stark and Bradley, 1999), the brain hemorrhage showed as hypointense on the T_2^*-weighted magnitude image (long solid arrow in Fig. 5a) and was surrounded by the typical dipole

pattern in the field map that was circular in axial view and of the shape of dumbbell in the coronal and sagittal views (Fig. 5b). Although there was no statistically significant difference over the entire brain between WL1 and WL2 ($P>0.05$), the WL2 reconstructed QSM displayed signal nonuniformities in the axial view (top, Fig. 5c) and streaking artifacts in the sagittal and coronal views (middle and bottom, Fig. 5c). These artifacts were markedly reduced in the corresponding WL1 reconstructed QSM (Fig. 5d). QSM provided an estimate of the susceptibility of the iron deposits in the hemorrhage and in the structures known to have high iron deposition such as the substantia nigra, basal gangelia and nucleus caudatus, and also provided an estimate of the susceptibility of deoxyhemoglobin in the veins. The ventricles (hollow arrows in Fig. 5) appeared slightly more hypointense than the globus pallidus (short arrows in Fig. 5) in the T_2^*-weighted magnitude images (Fig. 5a), but had substantially lower susceptibility than the globus pallidus in QSM (Fig. 5d).

Preliminary measurements of the susceptibilities at several regions in the brain were obtained in nine volunteers and are summarized in Table 1. The image scores (mean ± standard deviation) of QSMs by WL1 and WL2 were 1.8±0.4 and 2.9±0.3, respectively, which were statistically significant ($P<0.01$). The susceptibility values estimated by WL2 were slightly lower than that by WL1 ($P<0.01$) for regions with high susceptibility ($\chi \geq 0.1$) (substantia nigra, globus pallidus, and venous blood). The central regions of hemorrhages were measured to characterize susceptibility of this particular pathology; averaged susceptibility was 0.60 ± 0.15 ppm over four patients with hemorrhages using WL1 method.

Discussion

In this study, a physical prior based on structural consistency between the susceptibility map and the magnitude image is used to derive the susceptibility map from the magnetic field measured in a single orientation with gradient echo MRI. A weighted L_1 norm minimization is used to reduce streaking artifacts in the susceptibility map by minimizing edges in the susceptibility map that are not co-localized in the magnitude image. Simulations and controlled phantom experiments confirm that this morphology enabled dipole inversion (MEDI) approach to quantitative susceptibility mapping (QSM) is superior both in image quality and in quantification accuracy when compared to the previous weighted L_2 norm minimization method. It is shown that this MEDI QSM method is feasible for brain susceptibility mapping in patients including those with intracerebral hemorrhages.

Both the WL1 and WL2 methods are solved iteratively using the Lagrange multiplier formulation. For a fixed λ, the conjugate gradient solver in WL2 takes maximally 100 iteration to reach a solution, and the major computational burden in each iteration is the Fast Fourier Transform (FFT). On a personal computer with an Intel(R) Core™ i7 processor and 6 GB of memory, the calculation time was on the order of 1~2 minutes depending on the actual image size. In the WL1 method, the same CG solver was used to calculate the quasi-Newton iterations and usually 10~20 iterations are needed to reach the final solution, so the computational time is significantly elongated to about 20 minutes. By using the discrepancy principle, the Lagrange multiplier λ is chosen such that the residual error matches the noise. For each case, there may be a range of λ values that produce a residual error close to the expected noise level. The λ variation in a range may not significantly change the accuracy of the obtained susceptibility map (as demonstrated by the slope vs. λ curve in Fig. 1g), making the inversion fairly robust against choosing λ in practice. For the human imaging protocol used in this study, a constant $\lambda = 300$ was used in WL1 and generated susceptibility maps of good quality for all patients.

Through deconvolution of the dipole kernel, QSM substantially reduces the blurring of structures with high susceptibility in the phase image (Figs. 4b&d, 5b&d) and quantitatively

depicts tissue susceptibility. The average susceptibility values of the deep brain gray matter, including the globus pallidus, the putamen, the red nucleus and the substantia nigra, in nine volunteers are similar to those reported in previous works, summarized in Table 1 (Liu et al., 2011b; Schweser et al., 2011; Wharton et al., 2010). A proper formulation of prior information such as the proposed weighted L_1 minimization in this study is effective in removing artifacts in reconstruction and is more robust against corrupted phase data compared to weighted L_2 minimization as exemplified in Figs. 4c&d. This immunity to corrupted data largely explains the improvement in image quality over WL2, and may be crucial for clinical applications. The slight underestimation by WL2 has also been observed by others (Schweser et al., 2011), but a simple mathematical explanation remains to be found. While it is not possible to obtain histochemical correlation on susceptibility values obtained in vivo, susceptibility values estimated using the presented MEDI approach are in good agreement with (Liu et al., 2011b) to the previously developed COSMOS method (Liu et al., 2009), which uses multiple orientation sampling but does not require any prior information.

In the weighted L_1 based MEDI approach, as implemented in this feasibility study, the prior term in Eq. 3 may blur structures with low susceptibility value and low CNR in the magnitude images. The weak gradient leads to assignment of a nonzero weight in M, discouraging any spatial variation in the susceptibility through the prior term $MG\chi$. This is illustrated in the numerical simulations in the small tubes in the phantom in Fig. 1. Consequently, current weighted L_1 MEDI QSM may underestimate susceptibility in subtle structures with both low susceptibility and low CNR, such as the cortex gray matter region. However, even when the CNR is low, WL1 can quantify sources with high susceptibility whereas WL2 tends to underestimate (the outlier in Fig. 2c). This is because the penalization from the prior term $||MG\chi||_p^p$ is smaller when p=1 than p=2 for large variations, allowing WL1 to keep data fidelity at a lower cost. Additional anatomic images with improved CNR, resolution and structure definition such as T_1 and T_2 weighted images may be used to supply additional or improved edge information. This judicial use of high CNR images in combination with T_2^* magnitude images may improve the definition of the structural prior and correspondingly improve this QSM method.

Another source of error common to all quantitative susceptibility mapping methods is digitization error in the phase image for field map estimation. An accurate local field is essential for any QSM algorithm (de Rochefort et al., 2010; Liu et al., 2010; Schweser et al., 2010b). It has been noted that phase is sensitive to subject orientation (Schweser et al., 2011) and it has been suggested that an anisotropic imaging voxel will lead to underestimation (Haacke et al., 2010). The phase of a voxel measured in MRI is the phase of the complex signal summed over all different spins N_s in that voxel $\angle\Sigma_s N_s e^{i\gamma B_s TE}$, where the symbol $\angle$ denotes the phase of a complex number and B_s represents the magnetic field experienced by a particular spin. This is different from the average phase of spin isochromats of these materials $<\gamma B_s TE>$. The former is an approximation of the latter but is commonly used with little caution. The latter represents the average of the field in the voxel and is the quantity of interest in susceptibility mapping. High spatial resolution isotropic imaging is needed to reduce these digitization errors.

The susceptibility measured from vein of galen was 0.28 ± 0.02 ppm. With the knowledge of hematocrit value (Hct) and the susceptibility difference $\Delta\chi_{do}$ between oxygenated and fully deoxygenated blood, the susceptibility value could be converted to blood oxygen saturation levels. However, the hematocrit value varies among subjects, and there are several reported $\Delta\chi_{do}$ values in the literature ranging from 2.26ppm to 3.90ppm (Golay et al., 2001; Spees et al., 2001; Thulborn et al., 1982; Weisskoff and Kiihne, 1992) If we assume Hct=0.4, then $\Delta\chi$= 0.28ppm corresponds to an oxygen saturation level of 69% with

$\Delta\chi_{do}$=2.26ppm, or 82% with $\Delta\chi_{do}$=3.9ppm. The former value is in agreement with invasive measurements of oxygen saturation level ranging from 55% - 71% (Gibbs et al., 1942). Nevertheless, there are sources of uncertainty in the measured venous susceptibility. Flow effect was not fully compensated in the multi-echo gradient echo sequence for this study, which may have lead to an additional phase shift that cannot be accounted for by the dipole field.

QSM may be used to diagnose and characterize diseases and monitor interventions that involve biomarkers of strong magnetic susceptibility. These magnetic biomarkers include deoxyhemoglobin, iron depositions in neurodegenerative diseases, exogenously administered contrast agents such as gadolinium agents and superparamagnetic iron oxides, blood degeneration products such as hemosiderin arising from bleeding disorders including intracerebral hemorrhages and cerebral microbleeds and calcium depositions. QSM can be used to differentiate calcium deposits from iron deposits, and to quantify the amount of this magnetic biomarker, overcoming previous difficulties in the T_1&T_2 relaxation based approaches (Schabel and Parker, 2008; Stanisz and Henkelman, 2000; Terreno et al., 2006; Zurkiya et al., 2008). Such quantification of magnetic biomarkers by QSM may be very important for assessing disease severity and monitoring drug delivery.

While a rigorous theoretic proof regarding the accuracy of the MEDI approach is beyond the scope of this paper, the following insights into the dipole inversion may be worth noting. In the k-space formulation, susceptibility is well determined when the dipole kernel is not zero. Fortunately, the zeros of the dipole kernel are located on a double cone surface, making the susceptibility only slightly undersampled. Most susceptibility maps that generate the same field contain the typical undersampling streaking artifacts originating from strong susceptibility sources and noisy voxels, as well understood in CT (Kalender, 2006) and MRI radial sampling (Mistretta et al., 2006). Because such streaking is not considered to correspond to anything physical and radiates away from boundaries of objects in the images, a small amount of additional information may identify the true susceptibility map with the least streaking artifacts by imposing structural consistency with the simultaneously acquired magnitude image. This identification can be achieved by minimizing the number of voxels part of a gradient (or edge) of the candidate susceptibility map that are not part of a gradient (or edge) in the magnitude images. It may be possible that some voxels of the gradient of the true susceptibility map are not located on the gradient of the magnitude images, when the spin density variation coincidentally balances out the dephasing effects of the susceptibility variation in the magnitude images. In practice, these points may be far outnumbered by the points on streaking artifacts. Correspondingly, the L_1 minimization is effective in identifying a susceptibility map of minimal streaking artifacts as demonstrated in this study. Experimentally, preliminary data here and in the previous reported work (de Rochefort et al., 2010) have demonstrated that the Langrage multiplier λ is typically above 10^2, making the data fidelity term the dominant term in the cost function. This suggests that the physical prior's contribution to the determination of susceptibility may be secondary compared to that of the data fidelity term based on the phase data, which means only a small amount of additional information is needed in finding the susceptibility map with minimal artifacts.

The described weighted L_1 minimization is a substantial improvement over the previous weighted L_2 minimization for the MEDI approach in terms of image quality and susceptibility quantification, as summarized in Table 2. However, further theoretical investigation of the MEDI approach is required to elucidate its possibilities and limits. Since MEDI utilizes a spatial prior and phase images to reconstruct QSM, improvements in either the prior or the field estimation is expected to improve the final QSM. The method for assigning weights to edges in magnitude images may be improved by assigning probabilities to edges, instead of a binary decision. The formulation for sparsity promotion may be

improved for regions with poor CNR, such as regions with very large susceptibility and poor SNR or with very small susceptibility. Because MEDI QSM is a postprocessing method for gradient echo MRI, upon further refinement and stabilization, the MEDI algorithm should be compared with other processing methods such as R_2^* mapping and SWI (Haacke et al., 2004) and evaluated in pertinent applications to establish its clinical and scientific value.

Conclusions

In summary, for the morphology enabled dipole inversion approach to quantitative susceptibility mapping, a weighted L_1 minimization method is developed to identify the susceptibility map that is structurally consistent with the magnitude image. Numerical simulations and phantom experiments confirm that this weighted L_1 minimization method accurately measures susceptibility and suppresses typical undersampling streaking artifacts. This weighted L_1 minimization method is promising for clinical applications.

References

Bradley WG Jr. MR appearance of hemorrhage in the brain. Radiology. 1993; 189:15–26. [PubMed: 8372185]

Candes E, Romberg J. Sparsity and Incoherence in Compressive Sampling. Inverse Problems. 2007; 23:17.

de Rochefort L, Brown R, Prince MR, Wang Y. Quantitative MR susceptibility mapping using piece-wise constant regularized inversion of the magnetic field. Magn Reson Med. 2008a; 60:1003–1009. [PubMed: 18816834]

de Rochefort L, Liu T, Kressler B, Liu J, Spincemaille P, Lebon V, Wu J, Wang Y. Quantitative susceptibility map reconstruction from MR phase data using bayesian regularization: validation and application to brain imaging. Magn Reson Med. 2010; 63:194–206. [PubMed: 19953507]

de Rochefort L, Nguyen T, Brown R, Spincemaille P, Choi G, Weinsaft J, Prince MR, Wang Y. In vivo quantification of contrast agent concentration using the induced magnetic field for time-resolved arterial input function measurement with MRI. Med Phys. 2008b; 35:5328–5339. [PubMed: 19175092]

Ghiglia, DC.; Pritt, MD. Two-dimensional phase unwrapping: theory, algorithms, and software. Wiley; New York: 1998.

Gibbs EL, Lennox WG, Nims LF, Gibbs FA. Arterial and cerebral venous blood - Arterial-venous differences in man. Journal of Biological Chemistry. 1942; 144:325–332.

Golay X, Silvennoinen MJ, Zhou J, Clingman CS, Kauppinen RA, Pekar JJ, van Zij PC. Measurement of tissue oxygen extraction ratios from venous blood T(2): increased precision and validation of principle. Magn Reson Med. 2001; 46:282–291. [PubMed: 11477631]

Haacke EM, Cheng NY, House MJ, Liu Q, Neelavalli J, Ogg RJ, Khan A, Ayaz M, Kirsch W, Obenaus A. Imaging iron stores in the brain using magnetic resonance imaging. Magn Reson Imaging. 2005; 23:1–25. [PubMed: 15733784]

Haacke EM, Tang J, Neelavalli J, Cheng YC. Susceptibility mapping as a means to visualize veins and quantify oxygen saturation. J Magn Reson Imaging. 2010; 32:663–676. [PubMed: 20815065]

Haacke EM, Xu Y, Cheng YC, Reichenbach JR. Susceptibility weighted imaging (SWI). Magn Reson Med. 2004; 52:612–618. [PubMed: 15334582]

Hansen, PC. Rank-deficient and discrete ill-posed problems: numerical aspects of linear inversion. SIAM; Philadelphia: 1998.

Hestenes MR, Stiefel E. Methods of Conjugate Gradients for Solving Linear Systems. Journal of Research of the National Bureau of Standards. 1952; 49:409.

Jackson, JD. Classical electrodynamics. 3. John Wiley and Sons, inc; 1999.

Kalender, WA. Computed Tomography: Fundamentals, System Technology, Image Quality, Applications. Wiley, John & Sons, Inc; 2006.

Kressler B, de Rochefort L, Liu T, Spincemaille P, Jiang Q, Wang Y. Nonlinear regularization for per voxel estimation of magnetic susceptibility distributions from MRI field maps. IEEE Trans Med Imaging. 2010; 29:273–281. [PubMed: 19502123]

Li L, Leigh JS. Quantifying arbitrary magnetic susceptibility distributions with MR. Magnetic Resonance in Medicine. 2004; 51:1077–1082. [PubMed: 15122694]

Li W, Wu B, Liu C. Quantitative susceptibility mapping of human brain reflects spatial variation in tissue composition. Neuroimage. 2011; 55:1645–1656. [PubMed: 21224002]

Liu C. Susceptibility tensor imaging. Magn Reson Med. 2010; 63:1471–1477. [PubMed: 20512849]

Liu T, Khalidov I, de Rochefort L, Spincemaille P, Liu J, Tsiouris AJ, Wang Y. A novel background field removal method for MRI using projection onto dipole fields (PDF). NMR Biomed. 2011a

Liu T, Khalidov I, de Rochefort L, Spincemaille P, Liu J, Wang Y. Improved Background Field Correction Using Effective Dipole Fitting. Proc ISMRM. 2010:141.

Liu T, Liu J, de Rochefort L, Spincemaille P, Khalidov I, Ledoux JR, Wang Y. Morphology enabled dipole inversion (MEDI) from a single-angle acquisition: Comparison with COSMOS in human brain imaging. Magn Reson Med. 2011b

Liu T, Spincemaille P, de Rochefort L, Kressler B, Wang Y. Calculation of susceptibility through multiple orientation sampling (COSMOS): a method for conditioning the inverse problem from measured magnetic field map to susceptibility source image in MRI. Magn Reson Med. 2009; 61:196–204. [PubMed: 19097205]

Mistretta CA, Wieben O, Velikina J, Block W, Perry J, Wu Y, Johnson K, Wu Y. Highly constrained backprojection for time-resolved MRI. Magn Reson Med. 2006; 55:30–40. [PubMed: 16342275]

Nocedal, J.; Wright, SJ. Numerical optimization. 2. Springer; New York: 2006.

Salomir R, De Senneville BD, Moonen CTW. A fast calculation method for magnetic field inhomogeneity due to an arbitrary distribution of bulk susceptibility. Concepts in Magnetic Resonance Part B-Magnetic Resonance Engineering. 2003; 19B:26–34.

Schabel MC, Parker DL. Uncertainty and bias in contrast concentration measurements using spoiled gradient echo pulse sequences. Phys Med Biol. 2008; 53:2345–2373. [PubMed: 18421121]

Schweser F, Deistung A, Lehr BW, Reichenbach JR. Differentiation between diamagnetic and paramagnetic cerebral lesions based on magnetic susceptibility mapping. Med Phys. 2010a; 37:5165–5178. [PubMed: 21089750]

Schweser F, Deistung A, Lehr BW, Reichenbach JR. Quantitative imaging of intrinsic magnetic tissue properties using MRI signal phase: an approach to in vivo brain iron metabolism? Neuroimage. 2011; 54:2789–2807. [PubMed: 21040794]

Schweser F, Lehr BW, Deistung A, Reichenbach JR. A Novel Approach for Separation of Background Phase in SWI Phase Data Utilizing the Harmonic Function Mean Value Property. Proc ISMRM. 2010b:142.

Shmueli K, de Zwart JA, van Gelderen P, Li TQ, Dodd SJ, Duyn JH. Magnetic susceptibility mapping of brain tissue in vivo using MRI phase data. Magn Reson Med. 2009; 62:1510–1522. [PubMed: 19859937]

Spees WM, Yablonskiy DA, Oswood MC, Ackerman JJ. Water proton MR properties of human blood at 1.5 Tesla: magnetic susceptibility, T(1), T(2), T*(2), and non-Lorentzian signal behavior. Magn Reson Med. 2001; 45:533–542. [PubMed: 11283978]

Stanisz GJ, Henkelman RM. Gd-DTPA relaxivity depends on macromolecular content. Magn Reson Med. 2000; 44:665–667. [PubMed: 11064398]

Stark, DD.; Bradley, WGJ. Mosby. Magnetic Resonance Imaging. 3. Vol. III. 1999.

Terreno E, Geninatti Crich S, Belfiore S, Biancone L, Cabella C, Esposito G, Manazza AD, Aime S. Effect of the intracellular localization of a Gd-based imaging probe on the relaxation enhancement of water protons. Magn Reson Med. 2006; 55:491–497. [PubMed: 16450336]

Thulborn KR, Waterton JC, Matthews PM, Radda GK. Oxygenation dependence of the transverse relaxation time of water protons in whole blood at high field. Biochim Biophys Acta. 1982; 714:265–270. [PubMed: 6275909]

Vogel, CR. Computational methods for inverse problems. Society for Industrial and Applied Mathematics; Philadelphia: 2002.

Weisskoff RM, Kiihne S. MRI susceptometry: image-based measurement of absolute susceptibility of MR contrast agents and human blood. Magn Reson Med. 1992; 24:375–383. [PubMed: 1569876]

Wharton S, Bowtell R. Whole-brain susceptibility mapping at high field: a comparison of multiple- and single-orientation methods. Neuroimage. 2010; 53:515–525. [PubMed: 20615474]

Wharton S, Schafer A, Bowtell R. Susceptibility mapping in the human brain using threshold-based k-space division. Magn Reson Med. 2010; 63:1292–1304. [PubMed: 20432300]

Zurkiya O, Chan AW, Hu X. MagA is sufficient for producing magnetic nanoparticles in mammalian cells, making it an MRI reporter. Magn Reson Med. 2008; 59:1225–1231. [PubMed: 18506784]

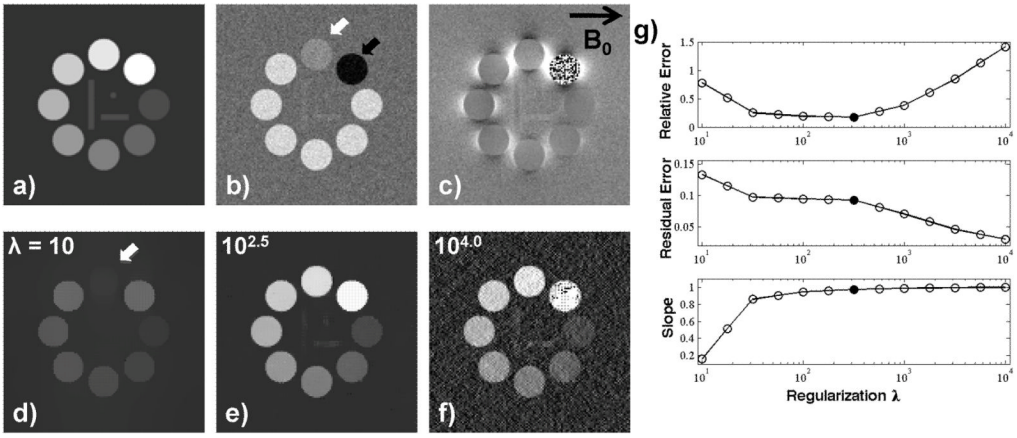

Figure 1.

Selection of the Lagrange multiplier λ and gradient mask threshold μ. **a)** Simulated susceptibility map, **b)** image magnitude, **c)** field map at a central section of a numerical phantom, **d–f)** QSM reconstructed with three λ values. and **g)** relative error, residual error and linear regression slope obtained with a range of λ ($10 \sim 10^{4.0}$). The optimal choice of λ ($10^{2.5}$, solid point in **g)** generated the minimal relative error. At this point, the residual error matched the noise level.

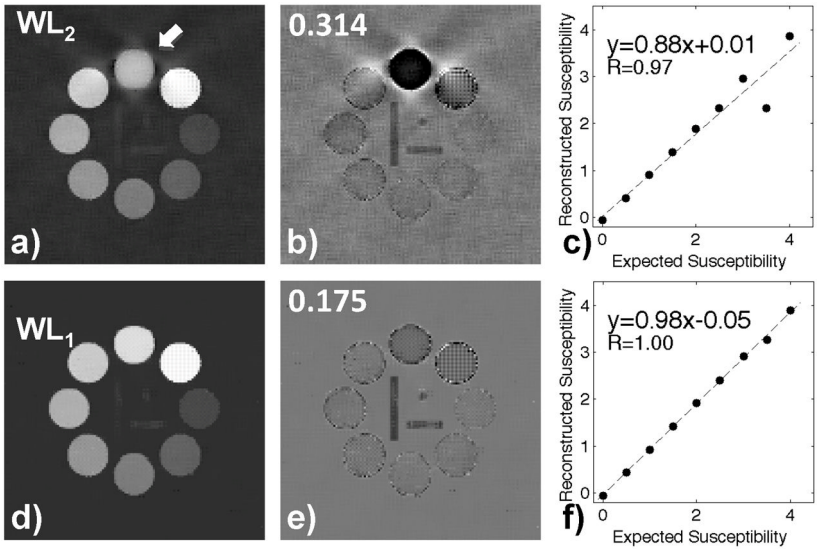

Figure 2.

Simulation validation of susceptibility maps obtained with weighted L_2 norm minimization (WL2, top row) and weighted L_1 norm minimization (WL1, bottom row). **a**&**d)** QSM, **b**&**e)** error map with the number in the top left corner indicating the relative error, and **c**&**f)** the linear regression between measured and know susceptibilities in the eight ROIs. In WL2 **(a)** substantial errors were observed in the region of low CNR. This region is indicated with a white arrow in **(a)** and corresponds to the outlier in **(c),** showing the underestimation error. The errors were reduced with WL1 **(d–f)**.

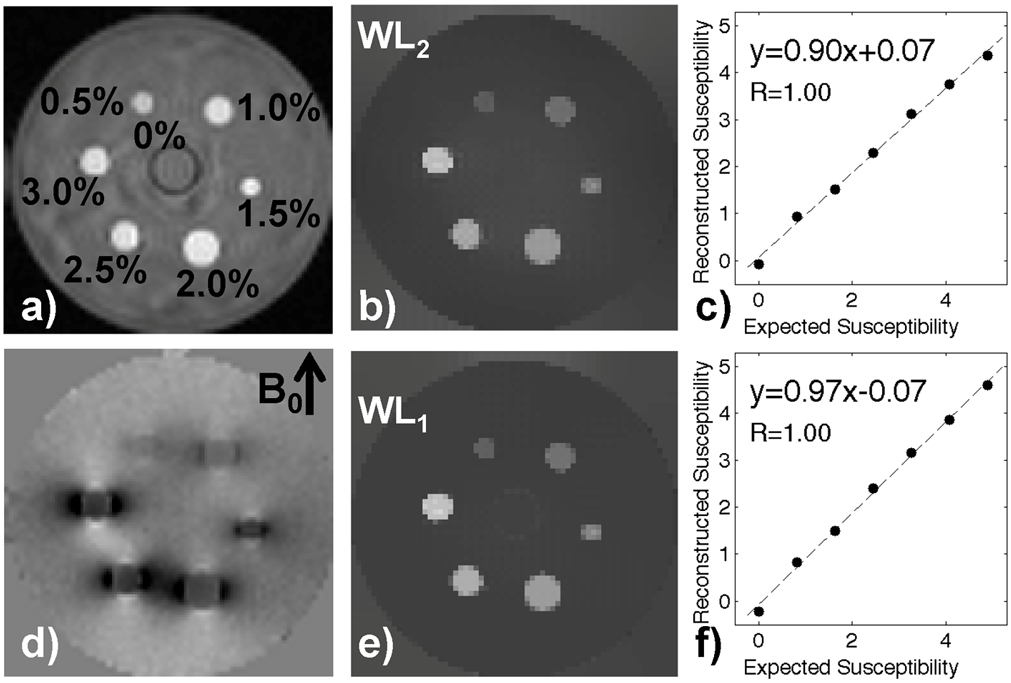

Figure 3.

Phantom experimental validation of QSMs reconstructed with WL2 and WL1 methods. **a)** Image magnitude, **d)** field map of a Gd-water phantom, **b**&**e)** QSMs reconstructed with WL2 and WL1 methods respectively, and **c**&f) linear regression plots between expected (prepared) susceptibilities and measured susceptibility from QSM, demonstrating that WL1 provides higher accuracy than WL2 (slope 0.97 vs 0.90).

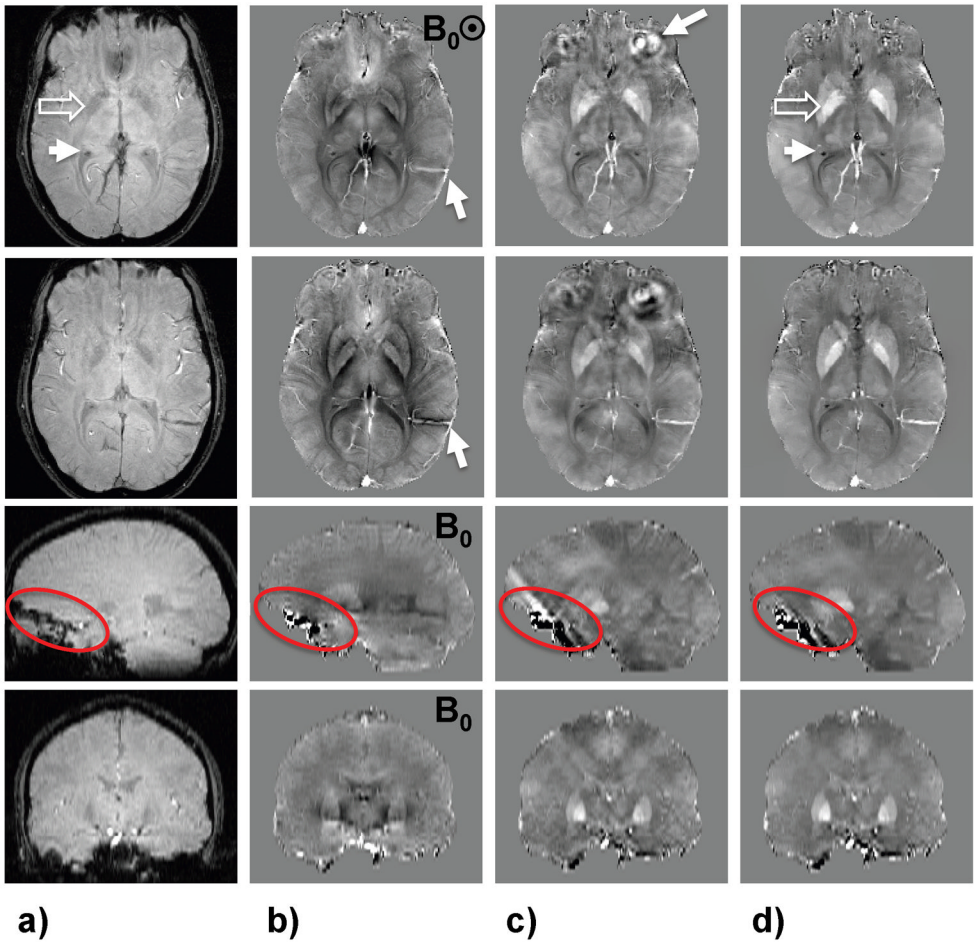

Figure 4.

Brain QSM of a healthy volunteer. **a)** Image magnitudes, **b)** field maps, **c)** QSMs reconstructed with WL2, and **d)** QSMs with WL1 displayed in two consecutive axial slices (top and second row), a sagittal (third row), and a coronal section (bottom row). Hypointense regions in the axial magnitude image included globus pallidus (hollow arrow in **a**) and ventricle (short arrow in **a**), which are indicated by the same arrows in **(d)**. An apparent vein in the field map is indicated by arrow in **(b)**. Artifacts as ringing in axial view and streaking in the sagittal view in the QSMs reconstructed with WL2 are indicated by arrow. The red oval in the third row highlights corrupted phase points at the boundary due to low SNR, the associated streaking artifacts on WL2, and their absence on WL1. The QSM reconstructed by WL1 **(d)** is considered to have substantially reduced streaking artifacts in the QSM by WL2 **(c)**.

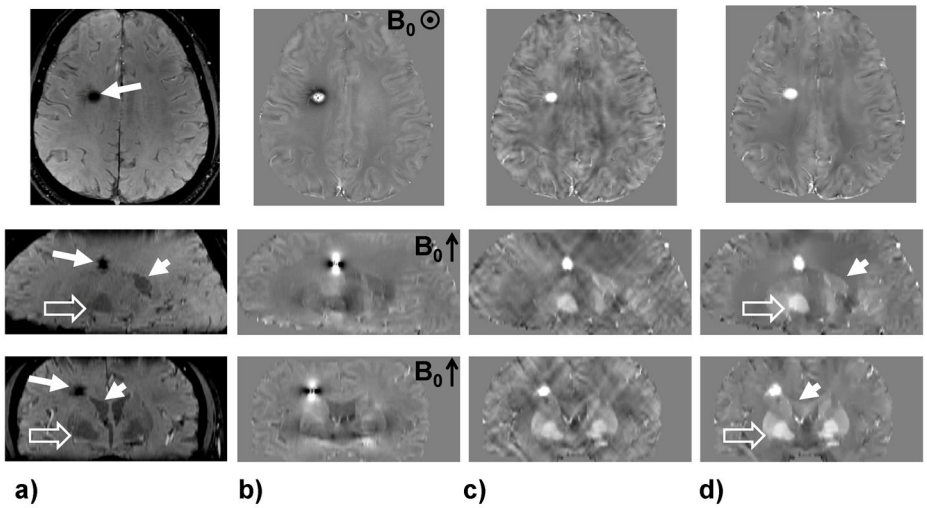

Figure 5.

QSM in the brain of a patient with a hemorrhage. **a)** Image magnitude, **b)** field map, **c)** QSM reconstructed with WL2, and **d)** QSM with WL1 displayed in axial (top row), sagittal (middle row), and coronal views (bottom row). Hypointense regions in the magnitude images include the globus pallidus (hollow arrows in **a & d**), the ventricles (short solid arrows in **a & d**) and a hemorrhage (long solid arrows in **a**).

Table 1

Susceptibility measurement of deep brain gay matter (unit in ppm). N indicates the number of subjects. The interval specified for each number indicates the inter-subject standard deviation, unless specified otherwise.

Method	N	Globus Pallidus	Putamen	Red Nucleus	Substantia Nigra	Venous blood
Single angle* (Schweser et al., 2011)	5	0.20±0.02	0.09±0.01	0.12±0.04	0.17±0.03	
COSMOS** (Schweser et al., 2011)	1	0.20±0.04	0.07±0.02	0.09±0.03	0.20±0.06	0.34±0.07
WL2 (current study)	9	0.16±0.02	0.08±0.02	0.07±0.04	0.10±0.03	0.25±0.03
WL1 (current study) (Liu et al., 2011b)	9	0.19±02	0.08±0.02	0.08±0.05	0.12±0.03	0.28±0.02
COSMOS(Liu et al., 2011b)	9	0.19±02	0.09±0.04	0.09±0.02	0.13±0.03	0.287±0.03
COSMOS (Wharton and Bowtell, 2010)	5	0.19±02	0.10±0.01	0.14±0.02	0.17±0.02	
Single angle (Wharton and Bowtell, 2010)***	5	0.19±02	0.09±0.01	0.13±0.02	0.16±0.03	

* after an empirical correction

** standard deviation measured over a region

*** another WL2 implementation of morphology enabled dipole inversion

Table 2

QSM quality of WL1 and WL2 implementations under various conditions.

Morphology (CNR)	Field (SNR)	Susceptibility	WL1	WL2
Reliable	Reliable	Any	+	+
Reliable	Unreliable(SNR≤3)	High	+	--
Unreliable(CNR≤3)	Reliable	High	+	−
Unreliable(CN≤3)	Reliable	Low	−	−

+ good depiction

−: blurring

--: streaking artifact